An alpaca nanobody neutralizes SARS-CoV-2 by blocking receptor interaction

Leo Hanke[1], Laura Vidakovics Perez[1], Daniel J. Sheward[1,4], Hrishikesh Das[2], Tim Schulte[3], Ainhoa Moliner-Morro[1], Martin Corcoran[1], Adnane Achour[3], Gunilla B. Karlsson Hedestam[1], B. Martin Hällberg[2, 5], Ben Murrell[1*] and Gerald M. McInerney[1*]

[1]Department of Microbiology, Tumor and Cell Biology, [2]Department of Cell and Molecular Biology and [3]Science for Life Laboratory, Department of Medicine Solna, Karolinska Institutet, and Division of Infectious Diseases, Karolinska University Hospital, Solna, Stockholm, Sweden. [4]Division of Virology, Institute of Infectious Diseases and Molecular Medicine, Faculty of Health Sciences, University of Cape Town, South Africa, [5]Centre for Structural Systems Biology, Notkestraße 85, 22607, Hamburg, Germany; Karolinska Institutet VR-RÅC

* These authors contributed equally.

For correspondence: Martin Hällberg (martin.hallberg@ki.se), Ben Murrell (benjamin.murrell@ki.se) and Gerald McInerney (gerald.mcinerney@ki.se).

Abstract

SARS-CoV-2 is the etiologic agent of COVID-19, currently causing a devastating pandemic for which pharmacological interventions are urgently needed. The virus enters host cells through an interaction between the spike glycoprotein and the angiotensin converting enzyme 2 (ACE2) receptor. Directly preventing this interaction presents an attractive possibility for suppressing SARS-CoV-2 replication. Here we report the isolation and characterization of an alpaca-derived single domain antibody fragment, Ty1, that specifically targets the receptor binding domain (RBD) of the SARS-CoV-2 spike, directly preventing ACE2 engagement. The nanobody binds with high affinity in the low nM range to the RBD, occluding ACE2. A cryo-electron microscopy structure of the bound complex at 2.9 Å resolution reveals that Ty1 binds to an epitope on the RBD accessible in both the 'up' and 'down' conformations and that Ty1 sterically hinders RBD-ACE2 binding. This 12.8 kDa nanobody does not need an Fc domain to neutralize SARS-CoV-2, and can be expressed in high quantities in bacteria, presenting opportunities for manufacturing at scale. Ty1 is therefore an excellent candidate as an intervention against COVID-19.

33 **Main**

34 SARS-CoV-2 emerged as the etiologic agent of COVID-19 in Wuhan, China in late 2019. In the
35 comparatively short time since then, it has achieved pandemic status, causing more than 7.3 million cases,
36 leading to at least 414,000 deaths and rising. Accordingly, the WHO declared the pandemic to be a public
37 health emergency of international concern. A safe and effective vaccine is urgently needed, but requires
38 time to develop. In the meantime, and indeed also in the post-vaccine era, highly specific and potent
39 antiviral interventions are needed. Many generic or repurposed candidates are in trials, but so far results
40 have been unremarkable. Since the virus is newly emerged, specifically designed drugs have not yet
41 reached late phase trials. When available, specific antiviral drugs or antibody therapies will be used to
42 protect individuals at risk and their widespread use will allow immunologically naïve populations to exit
43 lockdowns more safely.
44
45 The virus is closely related to SARS-CoV-1, both being members of the lineage 2 betacoronaviruses. Cell
46 entry of both viruses is achieved by first binding to the cell surface expressed receptor angiotensin-
47 converting enzyme 2 (ACE2), followed by conformational changes in the viral spike glycoprotein trimer
48 and subsequent membrane fusion. The affinity of SARS-CoV-2 receptor binding domain (RBD) for
49 ACE2 is considerably higher than that for SARS-CoV-1[1,2], supporting efficient cell entry and likely
50 contributing to pathogenesis. The RBD is a globular domain situated on the distal surface of the spike
51 protein. Two conformations have been observed in the stabilized trimer. Specifically, one conformation
52 where one RBD is ACE2-accessible while two are not and one conformation where all three RBDs are
53 down, i.e. receptor inaccessible[2,3]. As the receptor-engaging part of the spike, the RBD is an attractive
54 target for coronavirus neutralization, and a number of conventional neutralizing monoclonal antibodies
55 that target the RBD and block receptor binding have already been isolated from convalescent patients[4–6].
56
57 Camelid-derived single domain antibody fragments, also called VHHs or nanobodies, offer several
58 advantages over conventional antibodies as candidates for specific therapies. Despite being approximately
59 one tenth of the size of a conventional antibody, they retain specificity and affinity similar to conventional
60 antibodies while being far easier to clone, express and manipulate. They are readily expressed in bacteria
61 in large quantities and show high thermal stability and solubility, making them easily scalable and
62 extremely cost effective. Their modularity means that they can be oligomerized to increase avidity or to
63 increase serum half-life[7]. Critical to their use as antivirals in humans, they can easily be humanized with
64 existing protocols[8]. Importantly, they have proven to be highly potent inhibitors of viral infections in
65 vivo, particularly respiratory infections[9,10].
66

67 We immunized one alpaca with SARS-CoV-2 S1-Fc and RBD in a 60-day immunization schedule. We
68 generated a phage display library and performed two consecutive rounds of phage display, followed by an
69 ELISA-based binding screen (Fig. 1a). We isolated one nanobody, Ty1, that binds specifically to the
70 RBD of the SARS-CoV-2 spike glycoprotein. In parallel we performed next generation sequencing
71 (NGS) on the baseline and post-enrichment libraries, and quantified variant frequency before and after
72 each enrichment step. Ty1 exhibited the greatest fold-change in frequency among all nanobody variants,
73 increasing over 10,000-fold from baseline to after the second enrichment round (Fig.1b). We report the
74 amino acid sequence of Ty1 in Figure 1c.

75 To determine whether Ty1 neutralized SARS-CoV-2 we employed an *in vitro* neutralization assay using
76 lentiviral particles pseudotyped with the SARS-CoV-2 spike protein. Ty1 neutralized SARS-CoV-2
77 pseudotyped viruses at an IC_{50} of 0.77 μg/ml (54 nM) (Fig. 2a). No neutralization of a lentivirus
78 pseudotyped with VSV-G by Ty1 was evident, and a control nanobody produced and purified in the same
79 way, but specific for influenza A virus nucleoprotein[11] showed no evidence of neutralization of SARS-
80 CoV-2 pseudotyped viruses. When Ty1 was expressed in mammalian cells as a Fc-fusion protein the
81 potent neutralization could be further increased to ~5 ng/ml (Fig. S1).

82 To confirm that Ty1 is directed specifically against the SARS-CoV-2 spike protein, we characterized the
83 specificity of Ty1 by flow cytometry. We site-specifically conjugated a fluorophore to the C-terminus of
84 Ty1 by means of a Sortase A reaction and copper-free click chemistry (Ty1-AS635P) and stained
85 untransfected cells and cells transiently transfected with SARS-CoV-2 spike under permeabilizing
86 conditions (Fig. 2b). While untransfected and unstained cells displayed similar signals, cells expressing
87 the viral spike protein showed a strong shift in fluorescence intensity when stained with Ty1-AS635P.
88 The apparent double peak likely reflected the varying efficiency of this transient transfection. To
89 determine if the same probe can be exploited to recognize the viral spike protein in immunofluorescence,
90 we infected Vero E6 cells with infectious SARS-CoV-2 at MOI 1 for 24 hours and stained the fixed and
91 permeabilized cells with Ty1-AS635P and anti-dsRNA antibody (Fig. 2c). While uninfected cells showed
92 no signal, infected cells were strongly labelled with both dsRNA antibody and Ty1-AS635P. Thus, Ty1
93 recognized the viral spike glycoprotein with high specificity in its native conformation in SARS-CoV-2-
94 infected cells. Importantly, the low background in both experiments also suggested that Ty1 is a highly
95 specific and suitable tool for research, diagnostics and therapy.

96 To understand the mechanism of neutralization, we evaluated the effect of Ty1 on RBD binding to ACE2.
97 We site-specifically conjugated a fluorophore to the C-terminus of the RBD (RBD-AS635P) and used this
98 probe to stain ACE2 expressing HEK293T cells (Fig. 2d). Preincubation of RBD-AS635P with unlabeled

Ty1 resulted in a significant reduction of ACE2 staining, while preincubation with the control nanobody NP-VHH1 had no such effect. This result indicated that Ty1 directly prevents binding of SARS-CoV-2 RBD to its host cell receptor ACE2.

Specific and high-affinity binding of Ty1 to the RBD was also demonstrated in kinetic bio layer interferometry (BLI) experiments. Dipping of surface-immobilized nanobodies into monomeric RBD solutions at 550 nM yielded binding responses with fast association kinetics and amplitudes reaching 1.5 nm only for Ty1 but not NP-VHH1 (red and blue curves, respectively, in Figure 3a). Titration experiments performed under normal (280 mM) and high salt (680 mM) conditions revealed concentration-dependent kinetic response curves for binding of RBD to Ty1 (Figs. 3b and S2a, respectively). The derived semi-log concentration-response curves revealed sigmoidal line-shapes with fitted apparent K_D-values of 8 ± 1.5 and 13 ± 1.5 nm for binding at normal and high salt conditions, respectively. Local fits to individual sensorgrams applying the standard 1:1 binding model appeared reasonable for the association phases at lower to intermediate RBD concentrations, as well as for all dissociation curves when fits were allowed to stay above zero (grey lines Figs. 3b and S2a 1st panel). However, the model deviated from the observed data at higher RBD concentrations. Instead almost perfect fits were obtained when the same data were analyzed in terms of a Bayesian two-dimensional distribution of K_D and koff-rate constants to address heterogeneous ligand site populations on the sensor surface[12–14]. For the two titrations at low and high salt conditions, distinct peaks at K_D- and k_{off}-rate values of 5-9 nM and 4-5*10^{-3} s^{-1} were obtained (Fig. 3b and S2a 4th panel). In both conditions, a second elevated plateau with K_D- and k_{off}-rate values of about 7 nM and 1-4*10^{-7} contributed significantly to the observed sensorgrams. Since most high-affinity protein-protein interactions in the nM-range have dissociation rates in the 1*10^{-3} s^{-1} range[15], we attribute the first defined peak as the relevant Ty1:RBD interaction. The second broad plateau is likely caused by RBD competition and rebinding effects on the sensor surface, as well as heterogeneous ligand populations[14,16,17]. The orthogonal biophysical method isothermal titration calorimetry (ITC)[18] confirmed the high affinity binding of Ty1 to RBD with a K_D of 9 nM (with estimated bounds of 1 and 70 nM) characterized by an exothermic enthalpy of about -10 ± 0.5 kcal/mole (Fig. 3c, *left panel*). Exothermic binding was already evident from the three initial relatively constant negative spikes that were caused by the injection of Ty1 to RBD (Fig. 3c, *right panel*). The amplitude of the following three to four spikes returned to baseline demonstrating saturation of the available RBD sites by Ty1 binding. Notably, return to baseline was accompanied by the appearance of preceding positive spikes (Fig. 3c, *left panel* and Fig. S2b). These spikes were also detected when Ty1 was injected into the buffer (HBS) and thus treated as Ty1 dilution effects during data analysis. Injection of NP-VHH1 into RBD did not cause any binding or dilution heat changes above background noise. It

132 should be noted that the ITC measurements were performed at the lowest possible protein concentrations
133 to derive K_D-values in the low nM range, while still being able to detect interaction heat above
134 background noise signals that were at about -0.17 ucal/s (maximum spike amplitude) and ± 0.05 ucal/s,
135 respectively. Altogether, we concluded from these results that RBD bound to surface-immobilized Ty1
136 with high affinity of about 5-10 nM.
137
138 To understand the structural basis underlying the potent neutralization of SARS-CoV-2 we performed a
139 cryo-EM structure determination of the prefusion-stabilized spike ectodomain in complex with Ty1. The
140 cryo-EM reconstruction reaches an overall resolution of 2.9 Å (Fig. 4a; 0.143 FSC) with strong variation
141 of estimated local resolution from high resolution in the core of the spike trimer to relatively low
142 resolution in the top of the spike. Nevertheless, the current reconstruction clearly shows that the spike
143 retains only one main conformation with one RBD 'up' and two RBDs 'down'. Importantly, all three
144 RBDs are decorated in their upper parts with a Ty1 nanobody. The nanobodies retain a similar binding
145 orientation to the RBD whether the RBD is found in the 'up' or 'down' conformation (Fig. 4a,b). Primary
146 interactions with the RBD are through the CDRs. Specifically, CDR1 interacts with RBD T470 and
147 V483-E484 and CDR3 interacts with RBD Y449, F490 and Q493. Interestingly, CDR2 does not form any
148 interactions with the RBD, instead it stabilizes the conformation of CDR1 in the RBD bound mode and
149 thereby acts indirectly to potentiate the Ty1-RBD binding.
150
151 Since ACE2 can only be bound by an RBD in the 'up' conformation, the current cryo-EM reconstruction
152 clearly shows that ACE2 binding is sterically hindered from two sides (Fig. 4c). Specifically, ACE2
153 binding is blocked both by the Ty1 nanobody bound to the RBD in the 'up' conformation and the
154 neighboring RBD in the 'down' conformation. Hence, ACE2 binding is sufficiently hindered with any
155 two of the available three binding RBD sites in the spike trimer.
156
157 The current coronavirus pandemic has drastic consequences for the world's population, and vaccines,
158 antibodies or antivirals are urgently needed. Neutralizing antibodies can block virus entry at an early step
159 of infection and potentially protect individuals that are at high risk of developing severe disease. We
160 report the identification and characterization of a SARS-CoV-2 RBD-specific single domain antibody
161 fragment (nanobody) termed Ty1 that potently neutralizes the virus. We identified Ty1 by binding assay
162 after two consecutive rounds of phage display, simultaneously monitoring sequence enrichment by NGS.
163 Although Ty1 exhibited the greatest fold-enrichment in the NGS analysis, multiple additional nanobodies
164 exhibited enrichment of varying extent across both rounds. As the correlation between phage display
165 enrichment and neutralization is likely imperfect, further analyses of our libraries will likely yield other

potent SARS-CoV-2 neutralizing nanobodies. In addition to neutralization activity, we also show that Ty1 can be used as a detection reagent in flow cytometry and immunofluorescence demonstrating its suitability as a research tool and for diagnostics.

It should be noted that the nanobody Ty1 can be readily produced in bacteria at very high yield (in excess of 30 mg/L culture), making it an excellent candidate for a low-cost, scalable antiviral agent against SARS-CoV-2, and we provide the amino acid sequence, encouraging direct exploitation as such. While nanobodies capable of binding SARS-CoV-2 spike have recently been isolated, these were generated after SARS-CoV-1 spike immunization[19], or PCR maturation[20]. Also, in both cases a fusion to human Fc domain is required for neutralization of SARS-CoV-2, precluding expression in bacterial culture. Naive libraries of human single-domain antibodies (sdAbs) have also been screened to identify SARS-CoV-2 spike-specific nanobodies[21,22], but they lack detailed structural information. Ty1 represents the first single-domain antibody isolated from an animal specifically immunized with a SARS-CoV-2 protein.

Future work will aim to improve the potency and potential efficacy of Ty1 through various strategies. For example, mutational scanning may yield potency improvements to Ty1. Also, since Ty1 already neutralizes as a monomeric protein, the generation of homodimeric or trimeric fusion constructs is expected to further increase its neutralization activity. Indeed, fusion of Ty1 to a human IgG1-Fc dramatically improved the IC_{50} of this molecule, to approximately 5 ng/ml (Fig. S2). Additional strategies will explore linker-based constructs that chain multiple copies of Ty1 together, which may provide similar improvements in potency while retaining the possibility of being expressed in bacteria. Ty1 may additionally be a useful component of a bi-specific or tri-specific antibody, which could combine epitope specificities to increase the mutational barrier to viral escape. Based on our work, we hope that Ty1 will be investigated as a candidate for antiviral therapy.

Methods

Cells and virus. Vero E6 cells (ATCC-CRL-1586) and HEK293T cells (ATCC-CRL-3216) were maintained in Dulbecco's Modified Eagle Medium (Gibco) supplemented with 10% fetal calf serum and 1% Penicillin-Streptomycin and cultured at 37°C in a humidified incubator with 5% CO_2. A HEK293T cell line engineered to overexpress human ACE2 (HEK293T-ACE2) was generated by the lentiviral transduction of HEK293T cells. Briefly, lentiviruses were produced by co-transfecting HEK293T cells with a plasmid encoding VSV-G (Addgene cat#12259), a lentiviral Gag-Pol packaging plasmid (Addgene cat#8455), and a human ACE2 transfer plasmid. Virions were harvested from the supernatant, filtered through 0.45 µm filters, and used to transduce HEK293T cells. All cell lines used for experiments were

200 negative for *Mycoplasma* as determined by PCR. Infectious SARS-CoV-2[23] was propagated in Vero E6
201 cells and titrated by plaque assay.
202
203 **Proteins and probes.** The plasmid for expression of the SARS-CoV-2 prefusion-stabilized spike
204 ectodomain with a C-terminal T4 fibritin trimerization motif was obtained from[2]. The plasmid was used
205 to transiently transfect FreeStyle 293F cells using FreeStyle MAX reagent (Thermo Fisher Scientific).
206 The S ectodomain was purified from filtered supernatant on Streptactin XT resin (IBA Lifesciences),
207 followed by size-exclusion chromatography on a Superdex 200 in 5 mM Tris pH 8, 200 mM NaCl.

208 The RBD domain (RVQ – VNF) of SARS-CoV-2 was cloned upstream of an enterokinase cleavage site
209 and a human Fc. This plasmid was used to transiently transfect FreeStyle 293F cells using the FreeStyle
210 MAX reagent. The RBD-Fc fusion was purified from filtered supernatant on Protein G Sepharose (GE
211 Healthcare). The protein was cleaved using bovine enterokinase (GenScript) leaving a FLAG-tag at the
212 C-terminus of the RBD. Enzyme and Fc-portion was removed on HIS-Pur Ni-NTA resin (Thermo Fisher
213 Scientific) and Protein G sepharose (GE Healthcare) respectively, and the RBD was purified by size-
214 exclusion chromatography on a Superdex 200 in 50 mM Tris pH 8, 200 mM NaCl.

215 In addition, the RBD domain (RVQ – VNF) was cloned upstream of a Sortase A recognition site
216 (LPETG) and a 6xHIS tag and expressed in FreeStyle 293F cells as described above. RBD-HIS was
217 purified from filtered supernatant on His-Pur Ni-NTA resin, followed by size-exclusion chromatography
218 on a Superdex 200.

219 The nanobodies were cloned for expression in the pHEN plasmid with a C-terminal Sortase recognition
220 site (LPETG) and a 6xHIS tag. This plasmid was used to transform BL21 cells for periplasmic
221 expression. Expression was induced with 1 mM IPTG at OD600 = 0.6; cells were grown overnight at
222 30°C. Nanobodies were retrieved from the periplasm by osmotic shock and purified by Ni-NTA affinity
223 purification and size-exclusion chromatography.

224 For mammalian expression, the sequence encoding the nanobody Ty1 was cloned upstream of an human
225 IgG1. This plasmid was used to transiently transfect FreeStyle 293F cells using the FreeStyle MAX
226 reagent. The Ty1-Fc fusion was purified from filtered supernatant on Protein G Sepharose followed by
227 size-exclusion chromatography.

228 Biotinylated and fluorescent probes were generated using Sortase A as described here[24] and here[25]. In
229 brief, nanobodies were site-specifically biotinylated on the C-terminus using Sortase A 5M. Nanobody at
230 a concentration of 50 μM was incubated with sortase A 5M (5 μM), GGGK-biotin (200 μM) in 50 mM

231 Tris, pH 7.5, 150 mM NaCl, 10 mM $CaCl_2$, for 2 hours at 25°C. Unreacted nanobody and sortase was
232 removed with Ni-NTA resin and excess GGGK-biotin was removed using Zeba spin desalting columns
233 (0.5 mL, 7k MWCO, Thermo Fisher Scientific).

234 To generate the fluorescently labeled probes, first a dibenzocyclooctyne-amine (DBCO-amine, Sigma
235 Aldrich) was attached via sortase A to the nanobody or the RBD. (Reaction conditions: 50 µM RBD or
236 nanobody, 50 µM Sortase A 5M, 8 mM DBCO-amine in 50 mM Tris pH 7.5, 150 mM NaCl, 10 mM
237 $CaCl_2$, 2 hours, 25°C). Unreacted probe, sortase and excess DBCO-amine was removed using Ni-NTA
238 resin and PD-10 columns (GE Healthcare) respectively. Abberior Star 635P-azide (Abberior GMBH) was
239 attached to the DBCO-labeled proteins in a copper-free click chemistry reaction. Unreacted fluorophore
240 was removed on PD-10 column (RBD) or size-exclusion chromatography (nanobody).

241 **Alpaca immunization.** Alpaca immunization and phage display was performed similarly as described
242 here[26] and here[27]. In brief, the adult male alpaca Tyson at PreClinics, Germany, was immunized 4 times in
243 a 60-day immunization schedule. SARS-CoV-2 S1-sheep-Fc (Native Antigen Company, SKU:
244 REC31806) was used for the first two immunization, and SARS-CoV-2 RBD produced in FreeStyle 293F
245 cells was used for the last two immunizations.
246
247 **Library generation and nanobody isolation.** After the final boost, RNA was isolated from PBMCs
248 (RNA Plus mini kit, Qiagen). For cDNA synthesis, SuperScript III RT (Thermo Fisher Scientific) was
249 used with a combination of oligo(dT), random hexamers, or gene specific primers (AL.CH2,
250 ATGGAGAGGACGTCCTTGGGT and AL.CH2.2 TTCGGGGGGAAGAYRAAGAC)[27]. Nanobody
251 sequences were PCR amplified and cloned into a phagemid vector for expression as pIII fusion. TG1 cells
252 (Lucigen) were transformed with this library by electroporation.

253 Cells were inoculated with VCSM13 helper phage, and the resulting phage was enriched in two
254 consecutive rounds of phage display on RBD immobilized on magnetic beads. After the second round of
255 phage display, individual bacterial colonies were picked in a 96 well format, grown until OD = 0.6 and
256 nanobody expression was induced by addition of 1 mM IPTG. After 16 hours incubation at 30°C,
257 bacterial supernatant was used as primary detection reagent in an ELISA coated with RBD or S
258 ectodomain. Bound nanobodies were detected with anti-E tag (Bethyl laboratories) secondary antibody.
259 Positive clones were sequenced and cloned into the pHEN expression vector for further characterization.

260 **Amino acid sequence of Ty1**

261 MAQVQLVETGGGLVQPGGSLRLSCAASGFTFSSVYMNWVRQAPGKGPEWVSRISPNSGNIGYT
262 DSVKGRFTISRDNAKNTLYLQMNNLKPEDTALYYCAIGLNLSSSSVRGQGTQVTVSS
263
264 **Next generation sequencing (NGS) and analysis of nanobody libraries.** Plasmids from nanobody
265 libraries before enrichment, and after each enrichment step, were amplified for 13 cycles using Q5 High-
266 Fidelity 2X Master Mix (NEB) according to manufacturer's instructions, using primers:
267 CACTCTTTCCCTACACGACGCTCTTCCGATCTCTCGCGGCCCAGCCGGCCATGG and
268 GGAGTTCAGACGTGTGCTCTTCCGATCTACCGGCGCACCACTAGTGCA, annealing at 72°C.
269 Illumina indexing primers were added using an additional 9 cycles, with Kapa HiFi. Amplicons were size
270 selected using Agencourt AMPure XP beads (bead ratio: 1:1), and were pooled at ratios of 6:2:1 for
271 pre:post-1:post-2 libraries, to account for the reduction in diversity expected during enrichment, and
272 sequenced on an Illumina MiSeq using the MiSeq Reagent Kit v3 (2x300) MS-102-3003.

273 Paired-end reads were merged using USEARCH11[28], and then processed in the Julia language, primarily
274 using the NextGenSeqUtils.jl package[29]. Briefly, reads are trimmed of primer sequences, and
275 deduplicated, maintaining read frequencies. Variant frequencies are calculated as combined frequency of
276 any reads matching a variant within 3% nucleotide divergence, using a kmer-based distance
277 approximation for rapid database search. Any reads with counts >3 from the second enrichment library
278 are searched for their variant frequencies across all databases. When calculating enrichment, to avoid
279 zeros due to sampling and to regularize against over-sensitivity to low-frequency baseline variants, all
280 frequencies are increased by the reciprocal of the size of the pre-enrichment database.

281 **Neutralization Assay.** Pseudotyped viruses were generated by the co-transfection of HEK293T cells with
282 plasmids encoding the SARS-CoV-2 spike protein harbouring an 18 amino acid truncation of the
283 cytoplasmic tail[30], a plasmid encoding firefly luciferase, and a lentiviral packaging plasmid (Addgene
284 cat#8455) using Lipofectamine 3000 (Invitrogen). Media was changed 12-16 hours after transfection, and
285 pseudotyped viruses were harvested at 48- and 72-hours post transfection, filtered through a 0.45 µm
286 filter, and stored at -80°C until use. Pseudotyped virus neutralization assays were adapted from protocols
287 previously validated to characterize the neutralization of HIV [31], but with the use of HEK293T-ACE2
288 cells. Briefly, pseudotyped viruses sufficient to generate ~100,000 RLUs were incubated with serial
289 dilutions of nanobodies for 60 min at 37°C. Approximately 15,000 HEK293T-ACE2 cells were then
290 added to each well and the plates were incubated at 37°C for 48 hours. Luminescence was then measured
291 using Bright-Glo (Promega) per the manufacturer's instructions on a GM-2000 luminometer (Promega)
292 with an integration time of 0.3s.
293

294 **Flow Cytometry.** Cells were trypsinized and fixed in 4% formaldehyde/PBS and stained with RBD-
295 AS635P under non-permeabilizing conditions or with Ty1-AS635P under permeabilizing conditions.
296 Fluorescence was quantified using a BD FACSCelesta and the FlowJo software package.
297
298 **Immunofluorescence.** Vero E6 cells were seeded onto coverslips in a 24-well plate and incubated
299 overnight at 37°C/5% CO_2. Cells were infected with SARS-CoV-2 at a MOI of 1 for 24 h. Cells were
300 fixed with 4% (v/v) formaldehyde, permeabilized in 0.5% Triton X-100 and blocked in 5% horse serum.
301 Cells were incubated with anti-dsRNA antibody (1:2000, J2 Scicons) for 1 hour at room temperature
302 followed by 1 hour staining with the secondary antibody anti-mouse-Alexa Fluor 488 (1:2000, Thermo
303 Fisher Scientific), Hoechst (1:1000, Invitrogen) and Ty1-AS635P (0.05 µg/mL). Coverslips were
304 mounted in mounting media and images were obtained using Zeiss Axiovert microscope and processed
305 using Adobe Photoshop.
306
307 **Biophysical Biolayer interferometry (BLI) and isothermal titration calorimetry (ITC).** BLI was
308 performed using single-use high-precision streptavidin biosensors (SAX) on an eight-channel Octet RED
309 instrument according to manufacturer's protocols (Fortebio)[16]. Assays were performed in 2xPBS
310 comprising 0,05% Tween-20 (PBST). Biotinylated nanobodies Ty1 and NP-VHH1 were loaded at
311 concentrations between 30 and 250 nM followed by quenching using biocytin to reach final sensor loads
312 of between 0.15 and 0.7 nm. For the comparative binding test, the eight sensors were divided into two
313 sets, each comprising double sample as well as single reference and single control sensors. Sample and
314 reference sensors were loaded with respective nanobodies. The SAX control was only quenched. Loading
315 of the two sets was performed consecutively to reach similar immobilization levels, while subsequent
316 association and dissociation phases were performed simultaneously. For association, the sample and
317 control sensors were dipped into RBD, while the reference sensor was dipped into PBST. For titration
318 experiments, all sensors were loaded simultaneously. During association one of the sensors was used as
319 reference and only dipped into PBST. Raw data were pre-processed, analyzed and fitted by applying the
320 1:1 binding model as implemented in the manufacturer's software. Bayesian analysis to obtain the two-
321 dimensional distribution of K_D and k_{off} -rate values were performed using Evilfit[12–14]. The shown titration
322 data were processed applying reference sensor subtraction and Savitzky-Golay filter operations.

323 For ITC, proteins were exchanged to 2xHBS-buffer (50 mM HEPES, 300 mM NaCl, pH 7.5) and isolated
324 as single peak populations by Superdex-200 HR10/300 size-exclusion chromatography. ITC
325 measurements were performed using an ITC200 calorimeter (GE Healthcare). The cell temperature was
326 set to 37ºC and the syringe stirring speed to 750 rpm. Before each experiment, the RBD and nanobodies

were loaded into the cell and syringe at concentrations of 4 μM and 75 μM, respectively. Data and binding parameters were analyzed using the MicroCal PeakITC software (Malvern). The integrated heat versus molar ratio plots of the Ty1:RBD interactions were obtained by subtracting the Ty1 dilution heat uptake from the binding data. The NP-VHH1:RBD data were only baseline-corrected, since dilution effects were not evident.

Raw and processed BLI/ITC data were imported into Rstudio for visualization and further analysis[32–34]. Data along with analysis R scripts will be made publicly available via Github and/or DataDryad.

Cryo-EM sample preparation and imaging. Spike trimer (0.7 mg/ml) and Ty1 (1.3 mg/ml) were mixed in a 1:8 molar ratio and incubated on ice for 5 minutes. A 3-µl aliquot of the sample solution was applied to glow-discharged CryoMatrix holey grids with amorphous alloy film (Zhenjiang Lehua Technology) in a Vitrobot Mk IV (Thermo Fisher Scientific) at 4 degrees and 100% humidity (blot 10 s, blot force 3). Cryo-EM data collection was performed with EPU 2.7 (Thermo Fisher Scientific) using a Krios G3i transmission-electron microscope (Thermo Fisher Scientific) operated at 300 keV in the Karolinska Institutet 3D-EM facility. Images were acquired in nanoprobe EFTEM mode with a slit width of 10 eV using a GIF 967 energy filter (Ametek) and a K3 detector (Ametek) during 2.4 seconds with a dose rate of 4.1 e-/px/s resulting in a total dose of 38 $e^-/Å^2$ fractionated into 40 movie frames. Motion correction, CTF-estimation, fourier binning (to 1.02 Å/px), picking and extraction in 428 pixel boxes were performed on the fly using Warp [35].
A total of 13,589 micrographs were selected based on an estimated resolution cutoff of 4 Å and defocus below 2 microns. and 573,036 particles were picked by Warp. Extracted particles were imported into cryoSPARC v2.15.0[36] for 2D classification, 3D classification and non-uniform 3D refinement. The particles were processed with C1 symmetry throughout. After 2D classification (300 classes) 354,678 particles were retained and used to build three ab-initio 3D reconstructions. These were further processed for heterogeneous refinement that resulted in one reconstruction showing high-resolution structural features in the core of the spike. One round of homogenous refinement followed by non-uniform refinement resulted in a final reconstruction to an overall resolution of 2.9 Å (0.143 FSC) using 210,832 particles. To minimise the effects of loss of delocalised information due to tight boxing[37], the particles were re-extracted with 600 pixel box size. In addition, localized reconstruction[38] were performed using particles where all parts of the spike except the N-terminal domains, the RBDs and the nanobodies had been subtracted[39]. The combined effects of these three approaches significantly increased the level of density detail in the upper part of the spike.

Model building and structure refinement. A structure of the 2019-nCoV spike protein trimer[19] (PDB: 6VSB) was used as a starting model for model building. The model was extended and manually adjusted in COOT[40]. The Nanobody structure was homology modelled using SWISS-MODEL[41] taking PDB:5JMR[42] as a template. The missing regions of the RBD domains were built based on the RBD-ACE2 crystal structure (PDB: 6LZG)[43]. Structure refinement and manual model building were performed using COOT and PHENIX[44] in interspersed cycles with secondary structure and geometry restrained. All structure figures and all EM density-map figures were generated with UCSF ChimeraX[45].

Bibliography

1. Shang, J. *et al.* Cell entry mechanisms of SARS-CoV-2. *Proc. Natl. Acad. Sci. U. S. A.* **117**, 11727–11734 (2020).
2. Wrapp, D. *et al.* Cryo-EM structure of the 2019-nCoV spike in the prefusion conformation. *Science* **367**, 1260–1263 (2020).
3. Walls, A. C. *et al.* Structure, Function, and Antigenicity of the SARS-CoV-2 Spike Glycoprotein. *Cell* **181**, 281–292.e6 (2020).
4. Ju, B. *et al.* Human neutralizing antibodies elicited by SARS-CoV-2 infection. *Nature* (2020) doi:10.1038/s41586-020-2380-z.
5. Shi, R. *et al.* A human neutralizing antibody targets the receptor binding site of SARS-CoV-2. *Nature* (2020) doi:10.1038/s41586-020-2381-y.
6. Cao, Y. *et al.* Potent neutralizing antibodies against SARS-CoV-2 identified by high-throughput single-cell sequencing of convalescent patients' B cells. *Cell* (2020) doi:10.1016/j.cell.2020.05.025.
7. Bannas, P., Hambach, J. & Koch-Nolte, F. Nanobodies and Nanobody-Based Human Heavy Chain Antibodies As Antitumor Therapeutics. *Front. Immunol.* **8**, 1603 (2017).
8. Vincke, C. *et al.* General strategy to humanize a camelid single-domain antibody and identification of a universal humanized nanobody scaffold. *J. Biol. Chem.* **284**, 3273–3284 (2009).
9. Detalle, L. *et al.* Generation and Characterization of ALX-0171, a Potent Novel Therapeutic Nanobody for the Treatment of Respiratory Syncytial Virus Infection. *Antimicrob. Agents Chemother.* **60**, 6–13 (2016).
10. Cardoso, F. M. *et al.* Single-domain antibodies targeting neuraminidase protect against an H5N1 influenza virus challenge. *J. Virol.* **88**, 8278–8296 (2014).
11. Hanke, L. *et al.* The Antiviral Mechanism of an Influenza A Virus Nucleoprotein-Specific Single-Domain Antibody Fragment. *MBio* **7**, (2016).

392 12. Svitel, J., Balbo, A., Mariuzza, R. A., Gonzales, N. R. & Schuck, P. Combined affinity and rate
393 constant distributions of ligand populations from experimental surface binding kinetics and
394 equilibria. *Biophys. J.* **84**, 4062–4077 (2003).
395 13. Gorshkova, I. I., Svitel, J., Razjouyan, F. & Schuck, P. Bayesian Analysis of Heterogeneity in the
396 Distribution of Binding Properties of Immobilized Surface Sites. *Langmuir* **24**, 11577–11586 (2008).
397 14. Schuck, P. & Zhao, H. The Role of Mass Transport Limitation and Surface Heterogeneity in the
398 Biophysical Characterization of Macromolecular Binding Processes by SPR Biosensing. *Methods*
399 *Mol. Biol.* **627**, 15–54 (2010).
400 15. Pollard, T. D. A guide to simple and informative binding assays. *Mol. Biol. Cell* **21**, 4061–4067
401 (2010).
402 16. Abdiche, Y., Malashock, D., Pinkerton, A. & Pons, J. Determining kinetics and affinities of protein
403 interactions using a parallel real-time label-free biosensor, the Octet. *Anal. Biochem.* **377**, 209–217
404 (2008).
405 17. Kamat, V. & Rafique, A. Designing binding kinetic assay on the bio-layer interferometry (BLI)
406 biosensor to characterize antibody-antigen interactions. *Anal. Biochem.* **536**, 16–31 (2017).
407 18. Velazquez-Campoy, A., Leavitt, S. A. & Freire, E. Characterization of Protein-Protein Interactions
408 by Isothermal Titration Calorimetry. in *Protein-Protein Interactions* 35–54 (Humana Press, 2004).
409 19. Wrapp, D. *et al.* Structural Basis for Potent Neutralization of Betacoronaviruses by Single-Domain
410 Camelid Antibodies. *Cell* **181**, 1004–1015.e15 (2020).
411 20. Huo, J. *et al.* Structural characterisation of a nanobody derived from a naïve library that neutralises
412 SARS-CoV-2. (2020) doi:10.21203/rs.3.rs-32948/v1.
413 21. Chi, X. *et al.* Humanized Single Domain Antibodies Neutralize SARS-CoV-2 by Targeting Spike
414 Receptor Binding Domain. *bioRxiv* 2020.04.14.042010 (2020) doi:10.1101/2020.04.14.042010.
415 22. Wu, Y. *et al.* Identification of Human Single-Domain Antibodies against SARS-CoV-2. *Cell Host*
416 *Microbe* (2020) doi:10.1016/j.chom.2020.04.023.
417 23. Monteil, V. *et al.* Inhibition of SARS-CoV-2 Infections in Engineered Human Tissues Using
418 Clinical-Grade Soluble Human ACE2. *Cell* **181**, 905–913.e7 (2020).
419 24. Antos, J. M. *et al.* Site-Specific Protein Labeling via Sortase-Mediated Transpeptidation. *Curr.*
420 *Protoc. Protein Sci.* **89**, 15.3.1–15.3.19 (2017).
421 25. Witte, M. D. *et al.* Production of unnaturally linked chimeric proteins using a combination of
422 sortase-catalyzed transpeptidation and click chemistry. *Nat. Protoc.* **8**, 1808–1819 (2013).
423 26. Sosa, B. A. *et al.* How lamina-associated polypeptide 1 (LAP1) activates Torsin. *Elife* **3**, e03239
424 (2014).
425 27. Maass, D. R., Sepulveda, J., Pernthaner, A. & Shoemaker, C. B. Alpaca (Lama pacos) as a

426 convenient source of recombinant camelid heavy chain antibodies (VHHs). *J. Immunol. Methods*
427 **324**, 13–25 (2007).
428 28. Edgar, R. C. & Flyvbjerg, H. Error filtering, pair assembly and error correction for next-generation
429 sequencing reads. *Bioinformatics* **31**, 3476–3482 (2015).
430 29. Kumar, V. *et al.* Long-read amplicon denoising. *Nucleic Acids Res.* **47**, e104 (2019).
431 30. Rogers, T. F. *et al.* Rapid isolation of potent SARS-CoV-2 neutralizing antibodies and protection in
432 a small animal model. *bioRxiv* 2020.05.11.088674 (2020) doi:10.1101/2020.05.11.088674.
433 31. Sarzotti-Kelsoe, M. *et al.* Optimization and validation of the TZM-bl assay for standardized
434 assessments of neutralizing antibodies against HIV-1. *J. Immunol. Methods* **409**, 131–146 (2014).
435 32. Wickham, H. *ggplot2: Elegant Graphics for Data Analysis*. (Springer, 2016).
436 33. Wickham, H. tidyverse: Easily Install and Load the 'Tidyverse. (2017).
437 34. Team, R. C. R: A language and environment for statistical computing.
438 35. Tegunov, D. & Cramer, P. Real-time cryo-electron microscopy data preprocessing with Warp. *Nat.*
439 *Methods* **16**, 1146–1152 (2019).
440 36. Punjani, A., Rubinstein, J. L., Fleet, D. J. & Brubaker, M. A. cryoSPARC: algorithms for rapid
441 unsupervised cryo-EM structure determination. *Nat. Methods* **14**, 290–296 (2017).
442 37. Rosenthal, P. B. & Henderson, R. Optimal Determination of Particle Orientation, Absolute Hand,
443 and Contrast Loss in Single-particle Electron Cryomicroscopy. *Journal of Molecular Biology* vol.
444 333 721–745 (2003).
445 38. Ilca, S. L. *et al.* Localized reconstruction of subunits from electron cryomicroscopy images of
446 macromolecular complexes. *Nature Communications* vol. 6 (2015).
447 39. Morais, M. C. *et al.* Bacteriophage φ29 scaffolding protein gp7 before and after prohead assembly.
448 *Nature Structural & Molecular Biology* vol. 10 572–576 (2003).
449 40. Emsley, P., Lohkamp, B., Scott, W. G. & Cowtan, K. Features and development of Coot. *Acta*
450 *Crystallogr. D Biol. Crystallogr.* **66**, 486–501 (2010).
451 41. Waterhouse, A. *et al.* SWISS-MODEL: homology modelling of protein structures and complexes.
452 *Nucleic Acids Res.* **46**, W296–W303 (2018).
453 42. Dahms, S. O. *et al.* The structure of a furin-antibody complex explains non-competitive inhibition by
454 steric exclusion of substrate conformers. *Sci. Rep.* **6**, 34303 (2016).
455 43. Wang, Q. *et al.* Structural and Functional Basis of SARS-CoV-2 Entry by Using Human ACE2. *Cell*
456 **181**, 894–904.e9 (2020).
457 44. Adams, P. D. *et al.* PHENIX: a comprehensive Python-based system for macromolecular structure
458 solution. *Acta Crystallogr. D Biol. Crystallogr.* **66**, 213–221 (2010).
459 45. Goddard, T. D. *et al.* UCSF ChimeraX: Meeting modern challenges in visualization and analysis.

460 *Protein Sci.* **27**, 14–25 (2018).
461 46. Myszka, D. G., Jonsen, M. D. & Graves, B. J. Equilibrium analysis of high affinity interactions
462 using BIACORE. *Anal. Biochem.* **265**, 326–330 (1998).

463 **Acknowledgements**
464 SARS-CoV-2 virus was received from Jonas Klingström, KI. The authors thank James Voss and Deli
465 Huang for providing reagents. We thank Jason McLellan for providing the expression plasmid of the
466 stabilized SARS-CoV-2 spike protein. We thank PreClinics for their fast and efficient services as well as
467 Gunnar Schulte (KI), Per-Åke Nygren (KTH Stockholm) and Tomas Nyman (Protein Science Facility at
468 KI/SciLifeLabs) for providing access to BLI and ITC instruments. We also thank Fondation Dormeur,
469 Vaduz for generous support of flow cytometry equipment. This work was supported by an EU grant
470 (CoroNAb) to BM, GM and GBKH and by project grants from the Swedish Research Council to BM
471 (2018-02381), BMH (2017-6702 and 2018-3808) and to GM (2018-03914 and 2018-03843).
472

473 **Author Contributions**
474 L.H., L.V.P., D.J.S., T.S., A.M.M., M.C. and B.M. performed experiments and analyzed data. H.D. and
475 B.M.H. collected and processed cryo-EM data, built the model and performed the structural interpretation
476 of the data with the corresponding paper sections. A.A. and G.B.K.H. gave critical advice. L.H., B.M. and
477 G.M.M. conceived the study and wrote the initial draft. All authors contributed to the final draft.
478

479 **Competing Interests Statement**
480 The authors declare no conflicts of interest.
481

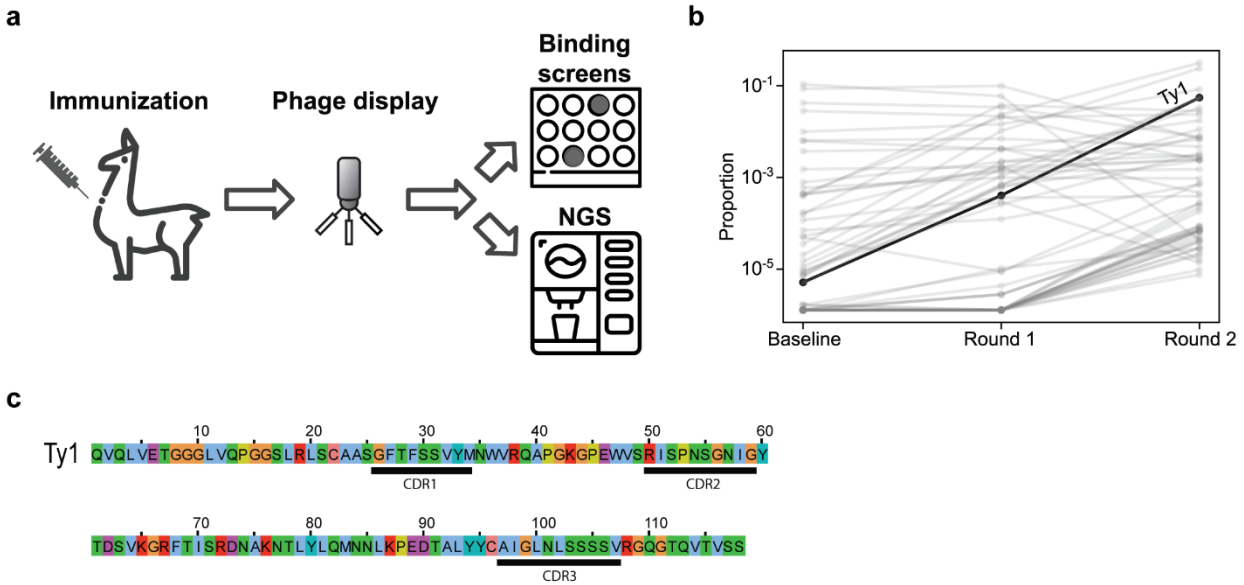

Figure 1 - Nanobody discovery.

a, Overview of the nanobody generation process. **b**, Variant frequencies quantified by NGS across successive enrichment steps. Identified using RBD bait, Ty1 exhibits the greatest total fold change of all nanobodies, increasing in proportion over 10,000-fold between initial and final libraries. **c**, Sequence of Ty1. Complementarity-determining regions (CDRs) are indicated. Color scheme according to ClustalX.

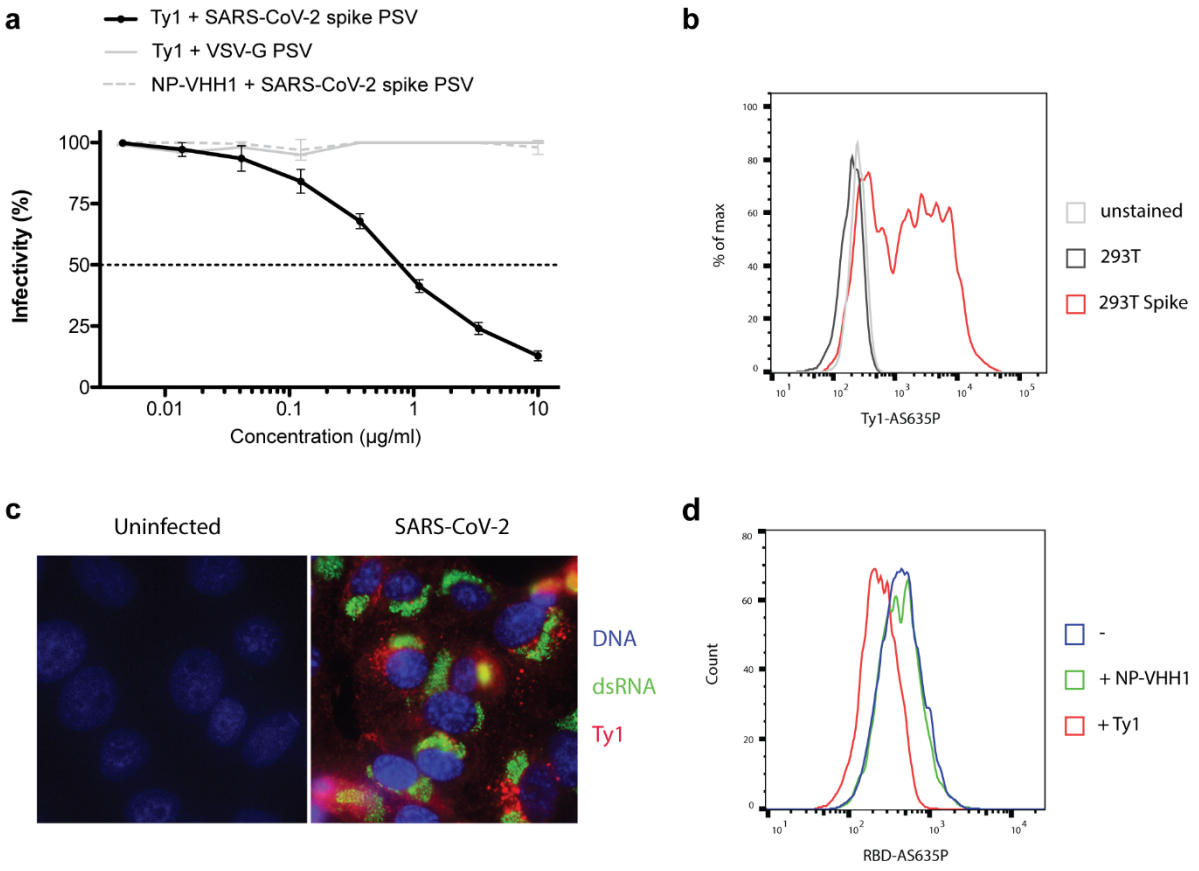

Figure 2 - Nanobody Ty1 neutralizes SARS-CoV-2 and specifically recognizes SARS-CoV-2 spike glycoprotein.

a, VSV G or SARS-CoV-2 spike pseudotyped lentivirus (PSV) was incubated with a dilution series of Ty1 or control nanobody (influenza NP-VHH1[11]). Infectivity relative to cells infected with pseudotyped virus in the absence of nanobody is shown. Neutralization by Ty1 was repeated in duplicate across 6 assays, and the error bars represent the standard deviation. **b**, Cells were transfected with a plasmid harboring the SARS-CoV-2 spike for 24 h. Cells were fixed, permeabilized and stained with Ty1-AS635P (black and red) or left unstained (grey). Cells were analyzed by flow cytometry. Cell counts are presented as % of max (representative histogram). **c**, Vero E6 cells were infected with SARS-CoV-2 at a MOI of 1 for 24 hours. Cells were fixed, permeabilized and stained for DNA (blue), dsRNA (green) and with Ty1-AS635P (red). Pictures were taken by fluorescence microscopy and representative examples are shown. **d**, ACE2 expressing HEK293T cells were trypsinized, fixed and stained with RBD-AS635P alone, or preincubated with IAV NP-VHH1 or Ty1. Cells were analyzed by flow cytometry.

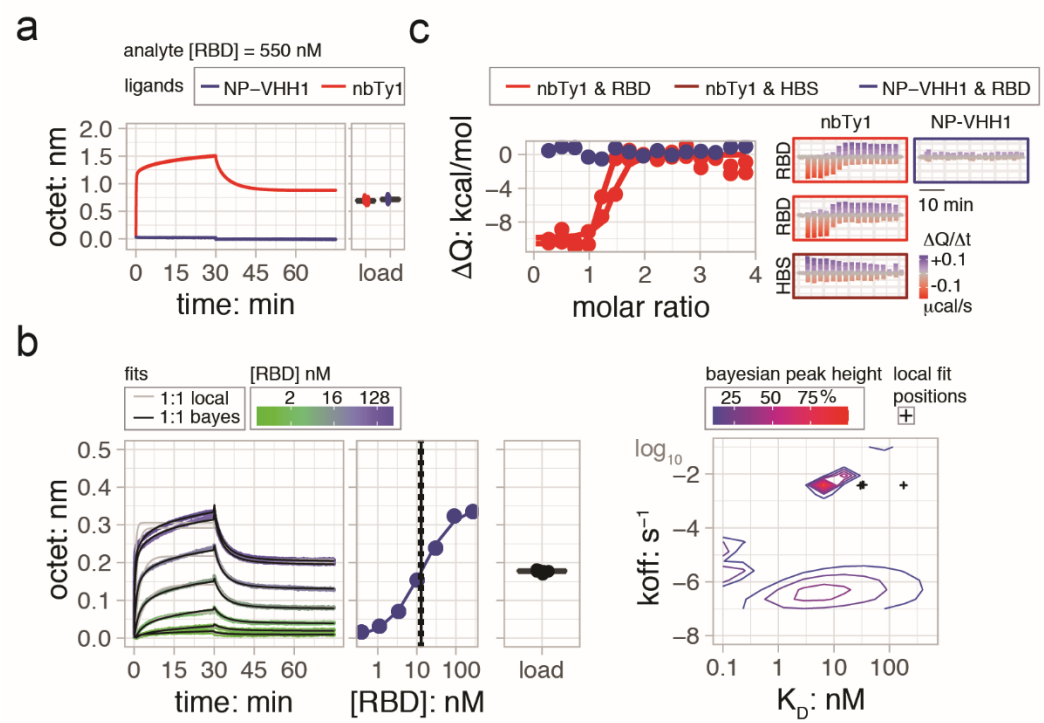

Figure 3 - RBD bound to Ty1 with 5-10 nM affinities in biophysical BLI and ITC measurements **a**, RBD bound to surface-immobilized Ty1 (red curves), but not to NP-VHH1 (blue curves). Almost equal nanobody immobilization levels of about 0.7 nm were obtained by first loading Ty1 and then NP-VHH1. In BLI, binding of molecules over time is recorded as sensorgrams recording the shift in wavelengths (unit: nm) due to an increase in the optical thickness of the surface layer. **b**, (1st panel) RBD titration sensorgrams obtained at high salt concentrations revealed concentration-dependent responses. Sensorgrams are color-coded according to the log2 RBD concentration scale. Standard and Bayesian 1:1 binding models are shown as grey and black solid lines. (2nd panel) Pseudo-equilibrium response values plotted against the logarithmic RBD concentration revealed sigmoidal binding curves that were fit to the single-site interaction model [46] yielding K_D-values in the low nM range. K_D-values and standard deviations are shown as solid and dotted lines, respectively. (3rd panel) Sensor immobilization levels are shown as jittered box plots. (4th panel) Two-dimensional distribution of dissociation rate (koff) and affinity (K_D) values obtained from the Bayesian and standard 1:1 model fits, visualized as densities according to depicted normalized height scale and single black crosses, respectively. *See related Figure S2A.* Plots for RBD/Ty1 titrations at low salt condition with same legends and scales. **c**, (1st panel) ITC demonstrated high affinity binding of Ty1 to RBD with fitted K_D– and binding enthalpy (DH) mean values of 9 nM (with estimated bounds of 1 and 70 nM) and -10 ± 0.5 kcal/mole, respectively, for two binding experiments (red). Injection of NP-VHH1 into RBD yielded heat changes at background level (blue). (2nd panel) Baseline-corrected heat changes plotted for two Ty1/RBD, a single Ty1/HBS buffer

524 and NP-VHH1/RBD titration experiments. Negative and positive heat changes are colored according to
525 the red-to-blue gradient. *See related Figure S2B:* Same figure on larger scale to highlight the Ty1 into
526 buffer dilution spikes.
527

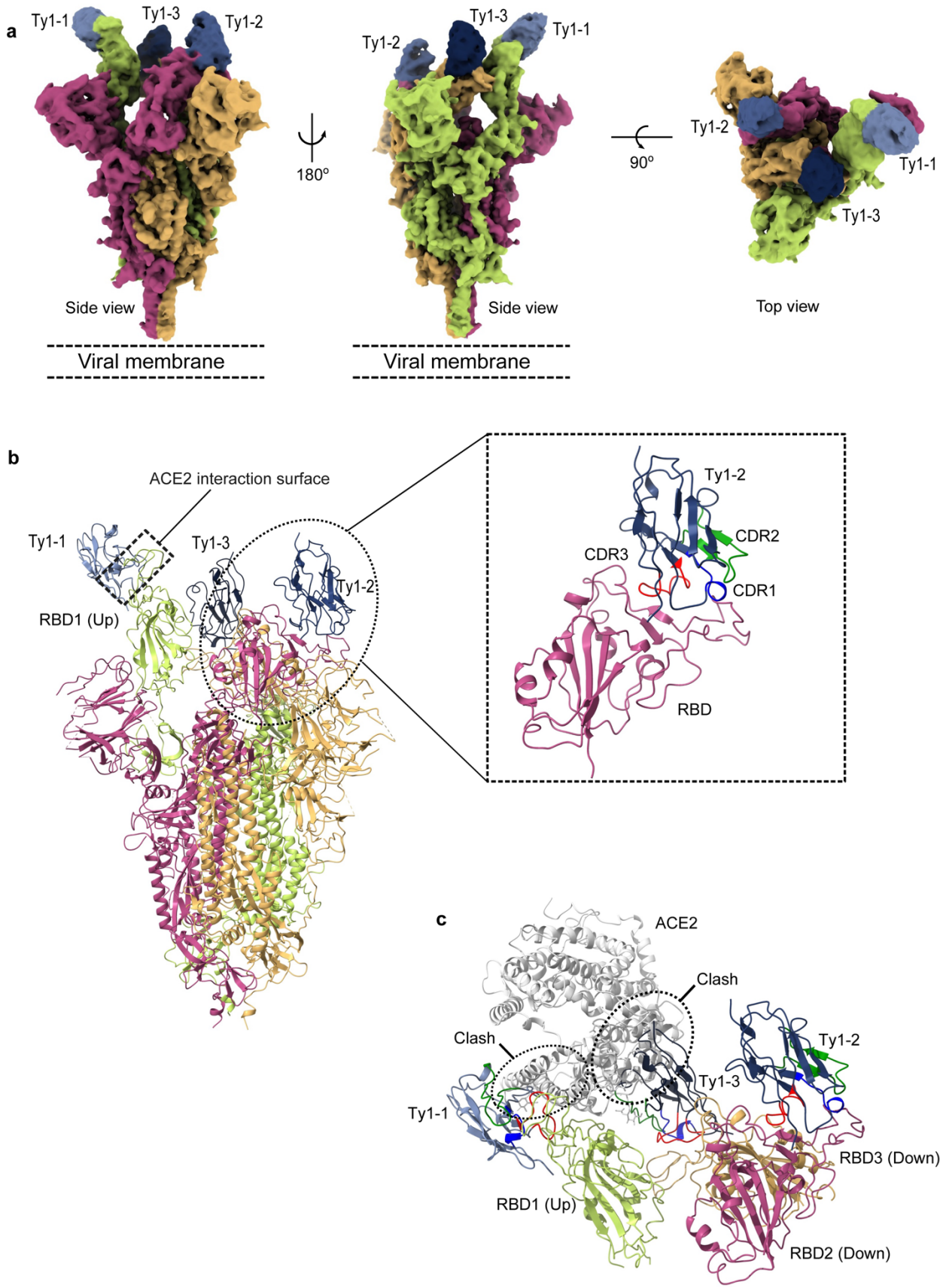
a
Ty1-1
Ty1-3
Ty1-2
Side view
Viral membrane
180°
Ty1-2
Ty1-3
Ty1-1
Side view
Viral membrane
90°
Ty1-2
Ty1-1
Ty1-3
Top view
b
ACE2 interaction surface
Ty1-1
Ty1-3
Ty1-2
RBD1 (Up)
Ty1-2
CDR2
CDR3
CDR1
RBD
c
ACE2
Clash
Clash
Ty1-2
Ty1-3
Ty1-1
RBD3 (Down)
RBD1 (Up)
RBD2 (Down)

528

Figure 4 - Ty1 binds to the RBD in 'up' and 'down' conformation and prevents ACE2 engagement

a, Cryo-EM reconstruction to an overall resolution of 2.9 Å (0.143 FSC) of the spike trimer with three bound molecules of Ty1. **b**, Atomic model (cartoon representation) of trimeric spike in complex with three molecules of Ty1. Three chains of spike are shown in three different colors. The RBD of chain A (light green) is present in 'up' conformation while the other two RBDs are captured in 'down' conformation. The ACE2 interaction surface of RBD1 and the Ty1 interaction surface is highlighted. Magnified view of RBD2 (in 'down' conformation) and Ty1 interaction is shown. CDR1,2 and 3 of Ty1 are shown in blue, green and red respectively. **c**, Ty1 shows a two-pronged inhibition of ACE2 receptor binding through binding the RBD in the 'up' conformation and by binding to the neighbouring RBD in the 'down' conformation. Binding of Ty1 to RBDs (both 'up' and 'down') would make ACE2 interaction surface inaccessible for ACE2.

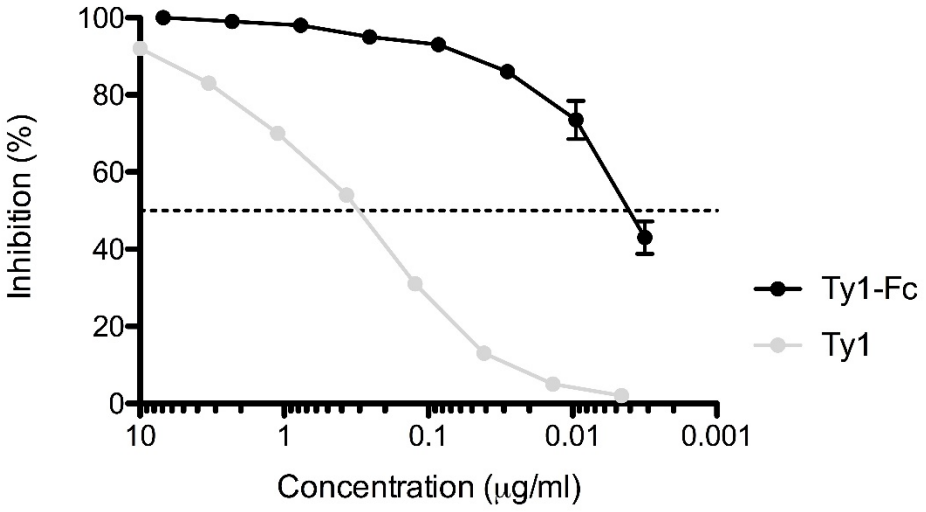

541

542 **Supplemental Figure 1 - Increased neutralization of a Ty1-Fc construct**

543 SARS-CoV-2 spike pseudotyped lentivirus (PSV) was incubated with a dilution series of Ty1 or Ty1-Fc.

544 Infectivity relative to cells infected with pseudotyped virus in the absence of nanobody is shown.

545 Neutralization was repeated in duplicate across 3 assays, and the error bars represent the standard

546 deviation

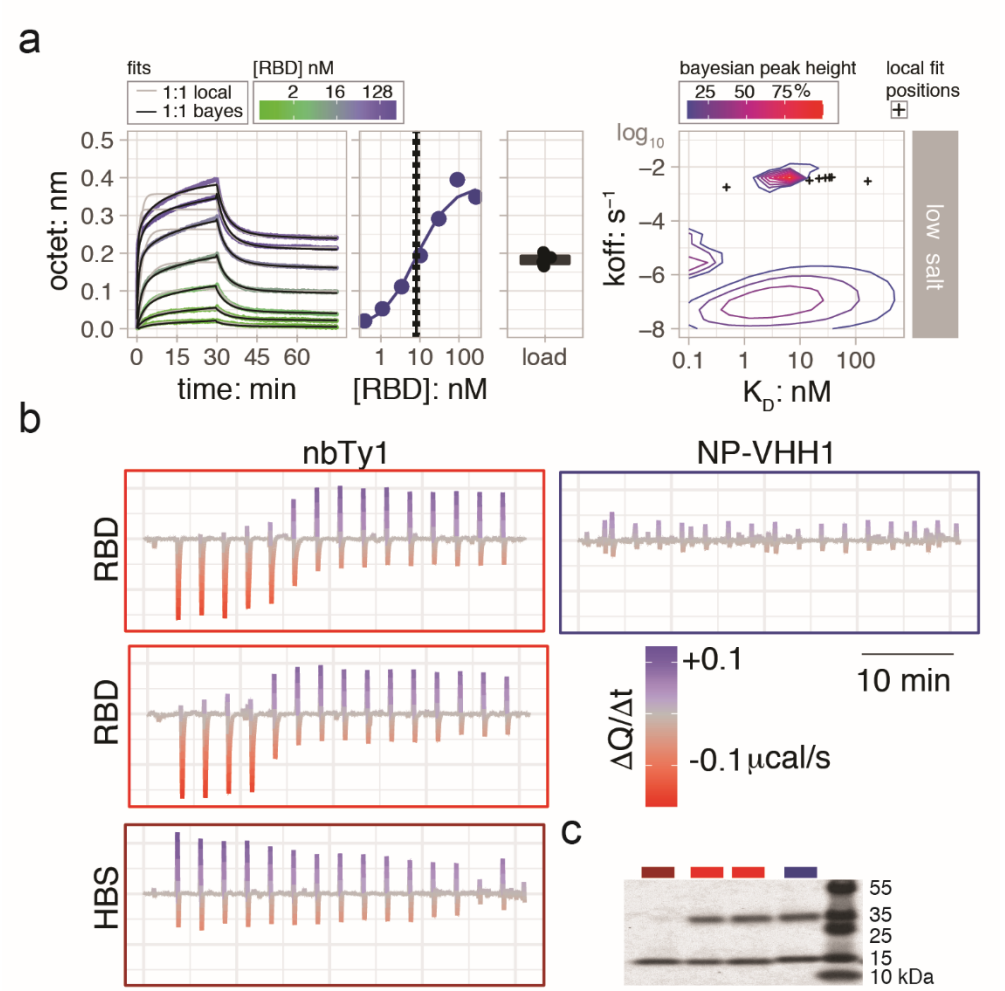

Supplemental Figure 2

a, related to Fig 3b, plots for RBD/Ty1 titrations at low salt condition with same legends and scales.

b, related to Fig 3c, Same data plotted on larger scale to highlight the Ty1 into buffer dilution spikes.

c, Samples after ITC were analyzed by SDS-PAGE.